Euro. Jnl of Applied Mathematics (2001), *vol.* 12, *pp.* 413–431. Printed in the United Kingdom

Flow in a double-film-fed fluid bead between contra-rotating rolls Part 2: bead break and flooding

M. J. GOSTLING[1], M. D. SAVAGE[1] and M. C. T. WILSON[2]

[1] *Department of Physics and Astronomy, University of Leeds, Leeds LS2 9JT, UK*
[2] *School of Mechanical Engineering, University of Leeds, Leeds LS2 9JT, UK*

(*Received 22 September 1999; revised 30 September 2000*)

Two-dimensional flow is considered in a fluid bead located in the gap between a pair of contra-rotating cylinders and bounded by two curved menisci. The stability of such bead flows with two inlet films, and hence no contact line, are analysed as the roll speed ratio S is increased. One of the inlet films can be regarded as an 'input flux' whilst the other is a 'returning film' whose thickness is specified as a fraction ζ of the outlet film on that roll. The flow is modelled via lubrication theory and for $Ca \ll 1$, where Ca represents the capillary number, boundary conditions are formally developed that account for $S \neq 1$ and the non-constant gap. It is shown that there is a qualitative difference in the results between the single and double inlet film models unless small correction terms to the pressure drops at the interfaces are taken into account. Futhermore, it is shown that the inclusion of these small terms produces an $O(1)$ effect on the prediction of the critical value of S at which bead break occurs. When the limits of the returning film fraction are examined it is found that as $\zeta \to 0$ results are in good agreement with those for the single inlet film. Further it is shown for a fixed input flux that as $\zeta \to 1$ a transition from bead break to upstream flooding of the nip can occur and multiple two-dimensionally stable solutions exist. For a varying input flux and fixed and 'sufficiently large' values of ζ there is a critical input flux $\bar{\lambda}(\zeta)$ such that as S is increased from zero:

(i) bead break occurs for $\lambda < \bar{\lambda}$;

(ii) upstream flooding occurs for $\lambda > \bar{\lambda}$;

(iii) when $\lambda = \bar{\lambda}$ the flow becomes neutrally stable at a specific value of S beyond which there exist two steady solutions (two-dimensionally stable) leading to bead break and upstream flooding, respectively.

1 Introduction

Part I of the investigation into flow in a Double-Film-Fed (DFF) fluid bead between contra-rotating rolls was concerned with the wide range of flow structures that arise and evolve as the control parameters are varied. A typical 3-roll coater, shown in figure 1 of part 1, illustrates the two distinct 'feed arrangements'. The lower gap is said to be double-film-fed since it is supplied by two inlet films. The upper gap, supplied by only one inlet film, is said to be Single-Film-Fed (SFF).

The aim of this paper is to explore the limits of operation of the DFF fluid bead imposed by the emergence of the bead break instability and by 'flooding' of the inlet. Bead break in a SFF fluid bead was investigated by Malone [9] and Kapur [6] by keeping the lower roll speed constant and gradually increasing, from rest, the speed of the upper roll. The upstream meniscus was observed to move inwards and through the nip (where the gap width is minimum) with the two-dimensional flow remaining stable. At a critical speed ratio the upstream meniscus becomes unstable and accelerates downstream; the bead rapidly contracts and bead break arises when the two menisci collide.

Kapur *et al.* [7] used lubrication theory to model the flow in the SFF bead and identified the presence of multiple solutions and a limit point for the existence of two-dimensional solutions. At this limit the flow becomes two-dimensionally unstable and marks the onset of the bead break instability. Three-dimensional perturbations to the two-dimensional bead flow were considered by Daniels [4] over a wide range of capillary numbers. In the meniscus coating regime, characterised by starved inlets and small capillary numbers ($Ca \ll 1$), his results showed there to be no three-dimensional instabilities; graphs of growth rate against wavenumber confirm that the most unstable waves are long waves – of zero wavenumber – on the upstream meniscus.

Rabaud *et al.* [13] observed DFF bead flow in the narrow gap between two non-concentric rotating cylinders when the total volume of fluid remains constant. The stability of both the upstream and downstream interfaces were investigated experimentally by Michelland [10] and Michelland *et al.* [11]. They showed the presence of the ribbing instability on the downstream meniscus – when the total volume of fluid is large – and a three-dimensional instability on the upstream when the volume of fluid is small. Reinelt [14] modelled the flow in this 'journal bearing' configuration and analysed its stability to small amplitude, three-dimensional perturbations. Of particular interest is the determination of the outgoing film thicknesses and the pressure jumps across each meniscus, which follows the work of Landau & Levich [8], Bretherton [3] and Park & Homsy [12], and includes corrections due to the varying gap width, unequal roll speed and the presence of thin films attached to the rolls. This analysis is put on a more rigorous basis in Appendix A.

In contrast to bead break, flooding occurs when the flux between the rolls becomes too large and there is a build up of fluid at the upstream interface. The flux through a moderately starved/flooded inlet has been studied experimentally [2] and the flooding of a DFF bead has also been investigated [1].

In the case of a SFF fluid bead, the higher order correction terms have no significant effect due to the difference in the $O(1)$ pressure terms being sufficiently large at the two interfaces. In the case of a DFF fluid bead, however, inclusion of such terms is found to be essential in order to model accurately the onset of bead break and inlet flooding.

§ 2 outlines the lubrication model employed in Part 1, but this is shown to be inadequate at the onset of bead break and model refinements, derived in Appendix A, are introduced. In § 3, results are presented for the limits $\zeta \to 0$ and $\zeta \to 1$.

2 Mathematical model

The DFF bead, with incoming/outgoing films of thickness H_1 and H_2 / H_3 and H_4 respectively, is shown in Figure 1. The rolls each have radius R and the fluid has viscosity

https://doi.org/10.1017/S0956792501004387 Published online by Cambridge University Press

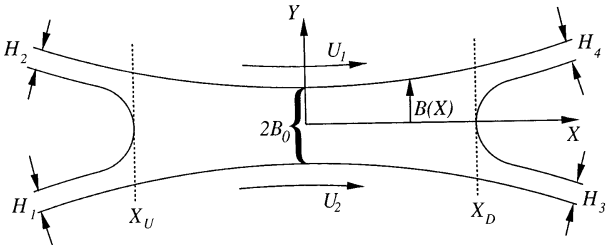

FIGURE 1. Double film fed bead between two adjacent rolls of a multiroll coater.

μ and surface tension σ. The mathematical model is similar to that in Part 1, with the system being described by several non-dimensional parameters: the roll speed ratio $S = U_1/U_2$; the capillary number $Ca = \mu U_2/\sigma$; the geometry ratio $\delta = \sqrt{B_0/2R}$; the returning film fraction $\zeta = H_2/H_4$; and the input flux $\lambda = Q_i/2B_0U_2$, where Q_i is the incoming flux on the lower roll. The value of ζ is a function of the size and operating conditions of all the subsequent rolls in the multiple roll system, and as such can vary between zero and unity. As this work is concerned with a single roll pair within a multi-roll system, ζ can be treated as an independent parameter.

The downstream meniscus position, x_d, and the flux, q, are determined in Part 1 via the Landau Levich relationship and a simple flux balance, whereas to find the upstream meniscus position, x_u, it is necessary to solve for the flow field. Since $\delta \ll 1$, the lubrication approximation is valid and this, along with no slip boundary conditions on the roll surfaces, leads to the Reynolds equation

$$\frac{dp}{dx} = \frac{3}{2b^3}[(1+S)b - 2q], \tag{2.1}$$

where p is the fluid pressure and $b = 1 + x^2 + O(\delta^2)$ is the gap width. This is a first order differential equation with *two* associated boundary conditions:

$$p(x_u) = -\Delta P_u(x_u) = -\frac{\delta}{b(x_u)Ca},\ p(x_d) = -\Delta P_d(x_d) = -\frac{\delta}{b(x_d)Ca}, \tag{2.2 a,b}$$

where $\Delta P_i = p_a - p(x_i)$, $i = u, d$, represent the pressure drops across the upstream and downstream interfaces, respectively, the radius of curvature at each meniscus is approximated by the associated semi-gap width and p_a is the ambient pressure, taken here to be zero. The problem is not over prescribed as (2.2 *a*) enables x_u to be found by forming the function $f(x)$:

$$f(x) = p(x) + \Delta P_u(x), \tag{2.3}$$

where x_u simply satisfies $f(x_u) = 0$. f is given explicitly by

$$\begin{aligned} f = \frac{3}{4}(1+S)\left[\theta - \theta_d + \frac{1}{2}\sin 2\theta - \frac{1}{2}\sin 2\theta_d\right] - \frac{3}{4}q\left[\frac{3}{2}\theta - \frac{3}{2}\theta_d + \right. \\ \left. \sin 2\theta - \sin 2\theta_d + \frac{1}{8}\sin 4\theta - \frac{1}{8}\sin 4\theta_d\right] + \Delta P_u(x) - \Delta P_d(x_d), \end{aligned} \tag{2.4}$$

where $x = \tan\theta$. The reader will note that x_d is also a root of f with the ΔP's defined by (2.2).

https://doi.org/10.1017/S0956792501004387 Published online by Cambridge University Press

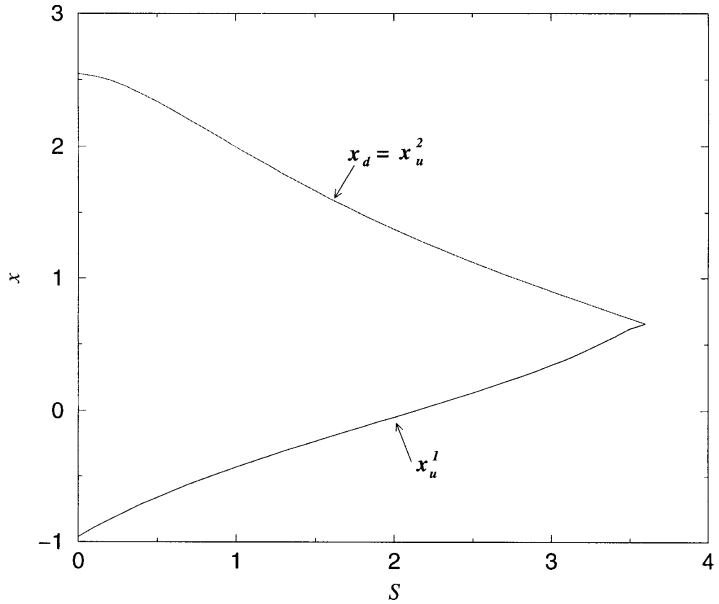

FIGURE 2. Mensicus positions against S for the DFF bead. $Ca = 10^{-3}, \delta = 5 \times 10^{-3}, \lambda = 0.05, \zeta = 0.5$.

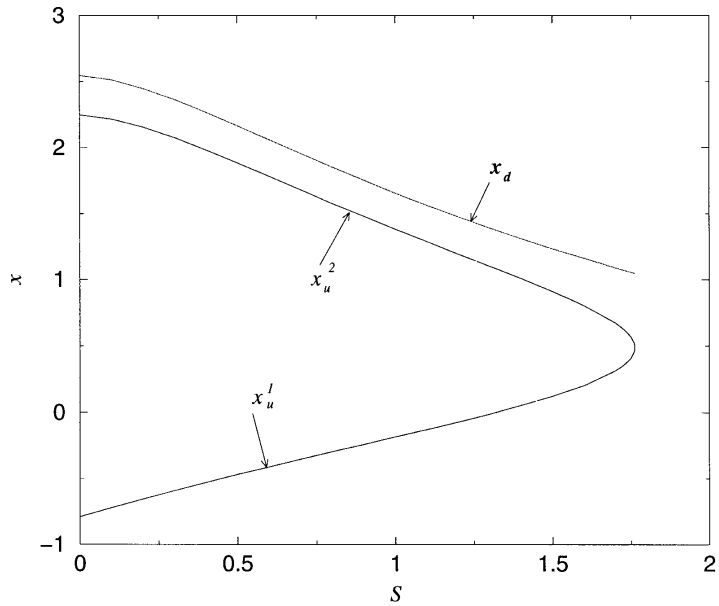

FIGURE 3. Meniscus positions against S for the SFF bead. $Ca = 10^{-3}, \delta = 5 \times 10^{-3}, \lambda = 0.05, \zeta = 0.5$.

A typical plot of upstream and downstream menisci position against S is shown in Figure 2, and it is interesting to compare this with the situation in the SFF case in Figure 3, analysed by Kapur *et al.*, where h_2 is replaced by a contact line. The differences are clear:

https://doi.org/10.1017/S0956792501004387 Published online by Cambridge University Press

- for a given value of S, the SFF model has two values of the upstream meniscus location – both *distinct* from x_d – with one being stable (i.e. seen in practice) and the other unstable. In the DFF model there are two roots x_u^1 and x_u^2, one of which is *coincident* with x_d (and hence non-physical).
- In the SFF case the variation of x_u with S exhibits a smooth turning point yet in the DFF case the x_u and x_d solution curves appear to meet in a corner. This apparent meeting of the menisci is a non-physical phenomenon, and furthermore, lubrication theory is no longer strictly valid in this regime as the X and Y lengthscales associated with the bead become comparable.

These differences could not easily be explained and led to a re-examination of the expressions employed for both the pressure drops and the outgoing film thicknesses.

Model refinements

The aim of the analysis in Appendix A is to derive more accurate representations for the film thicknesses and the pressure drops across the menisci. By including higher order terms, the analysis builds on the work of Park & Homsy [12] and rigorously confirms the results of Reinelt [14] to give the outgoing film thicknesses, scaled with B_0, as:

$$h_3 = 1.337 b_d (1 + 2x_d\delta) Ca^{2/3}, \tag{2.5}$$

$$h_4 = 1.337 b_d (1 + 2x_d\delta) S^{2/3} Ca^{2/3}, \tag{2.6}$$

and the pressure drops across each interface:

$$p(x_d) = -\Delta P_u = -\frac{\delta}{b_d Ca}\left(1 - 2x_d\delta + 1.94(1 + S^{2/3})Ca^{2/3}\right), \tag{2.7a}$$

$$p(x_u) = -\Delta P_d = -\frac{\delta}{b_u Ca}\left(1 + 2x_u\delta + \frac{\lambda}{b_u}\mathscr{A}_1 + \frac{1.337\zeta b_d S^{2/3}}{2b_u}\mathscr{A}_2 Ca^{2/3}\right), \tag{2.7b}$$

where

$$\mathscr{A}_i = \mathscr{A}_i(\mathscr{B}_i), \quad \mathscr{B}_1 = \frac{2\lambda}{(3Ca)^{2/3} b_u}, \quad \mathscr{B}_2 = \frac{0.643 b_d \zeta}{b_u}.$$

The higher order terms can simply be thought of as corrections to the radii of curvature of the interfaces, the $O(\delta)$ terms due to the non-constant gap width and the $O(Ca^{2/3})$ terms taking into account the presence of the thin films. x_d and x_u are solved for as before with f remaining as defined in (2.3) and (2.4), the only difference being in the definitions of the ΔP's.

Stability analysis

Daniels [4] demonstrated that for small capillary numbers in the case of the SFF bead, the upstream interface could become two- rather than three-dimensionally unstable. These results were supported by the experiments of Kapur [6], who demonstrated that when the speed ratio S is increased from zero, a critical value is reached at which the bead

https://doi.org/10.1017/S0956792501004387 Published online by Cambridge University Press

collapses. The instability leading to the collapse is thought to be two-dimensional as no three-dimensional disturbances (in the axial direction) were observed. Further verification is provided by Kapur *et al.* [7], whose two-dimensional linear stability analysis of the SFF bead demonstrated that, for sufficiently small Ca, the growth rate was directly proportional to

$$-\left(\frac{dp}{dx}|_{x_u} + \Delta P_u(x_u)\right),$$

i.e. the bead is deemed to be stable if and only if

$$\frac{df}{dx}|_{x_u} > 0. \tag{2.8}$$

As this paper deals with the small capillary number limit, this is the criterion adopted here to determine the stability or otherwise of the bead.

3 Results

3.1 Effect on meniscus locations and S_c

Figure 4 shows a typical plot of menisci positions against speed ratio S, and it allows the effect of the small terms to be seen. The dashed line represents the Leading Order Model (LOM) where the correction terms are neglected and the solid line represents the refined Higher Order Model (HOM). As S is increased from zero, both models predict that the menisci move towards each other, and in each case there is a maximum value of S, S_c say, beyond which no two-dimensional steady state solutions exist. S_c represents the point at which the two roots of f become one, hence the gradient of f is zero here. Therefore, according to (2.8), the bead is neutrally stable at this point, and thus S_c is associated with the critical speed ratio at which the bead collapses. The reader will note that this result indicates that the LOM predicts a bead of infinitesimal width to be stable which is clearly unphysical, and so provides further motivation for deriving the HOM. It is clear that at relatively low values of S the correction terms play a minor role as the differences between the predictions of the two models is minimal. However, as S_c is approached the predictions begin to differ more substantially, culminating in a 20% difference in the predicted value of S_c. Furthermore, for each S the HOM produces two values of x_u, each distinct from x_d, and the corner is replaced by a smooth turning point. Thus, the addition of the small terms produces results similar in form to the SFF model and significantly alters the prediction of S_c, and hence the critical operating conditions. This fundamental difference in the form of the solution given by the two models can be understood by analysing the function f and introducing two new functions, f_d and f_u, defined by:

$$f_d = p + \Delta P_d(x), \tag{3.1}$$

$$f_u = p + \Delta P_u(x). \tag{3.2}$$

The form of the ΔP's differ in each model; for the LOM they are defined by (2.2) and for the HOM they are given by (2.7). It can be shown [5] that the gradient of the x_u

https://doi.org/10.1017/S0956792501004387 Published online by Cambridge University Press

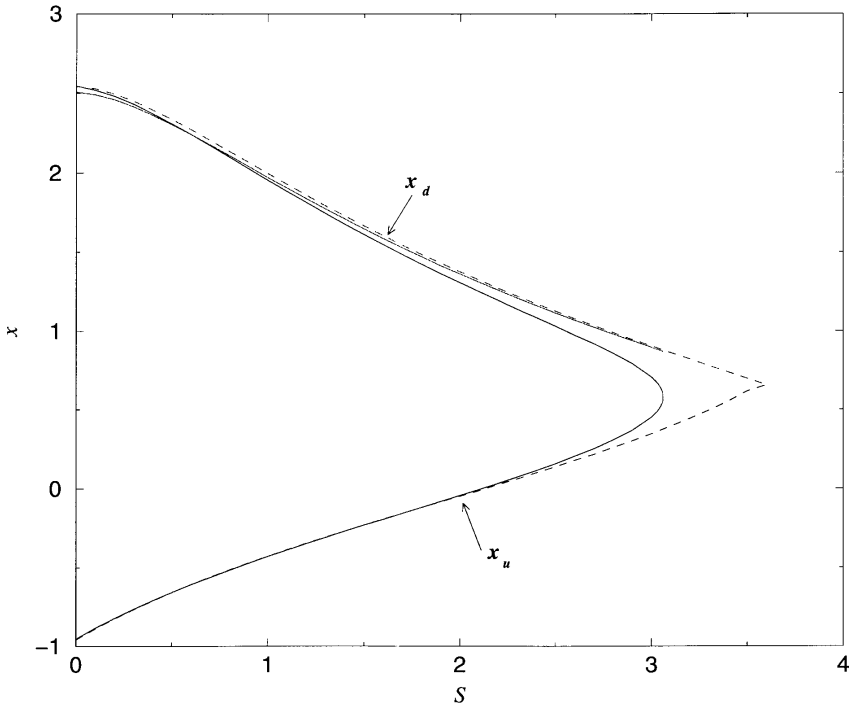

FIGURE 4. Menicus positions against S. Solid line: HOM; dashed line: LOM. $Ca = 10^{-3}, \delta = 5 \times 10^{-3}, \lambda = 0.05, \zeta = 0.5$.

solution curve is given by

$$\frac{dx_u}{dS} = \frac{\frac{\partial f_d}{\partial x}|_{x_d} \frac{\partial x_d}{\partial S} + \frac{\partial \Delta P_d}{\partial S}|_{x_u} - \frac{\partial \Delta P_u}{\partial S}|_{x_u}}{\frac{\partial f_u}{\partial x}|_{x_u}}. \tag{3.3}$$

Note that for the LOM the ΔP's are equal and so the last two terms of the numerator cancel. Moreover, for the LOM the f's are equal and $x_u^2 = x_d$, therefore at S_c (where $x_u^1 = x_u^2$ and the gradient of f is zero) the gradient of the x_u solution curve will remain finite and proportional to $\partial x_d/\partial S$. However, for the HOM the introduction of the small terms means that the ΔP's and f's are no longer equal, thus unlike the denominator, the numerator is not zero at S_c and the x_u solution curve will have an infinite gradient and hence a smooth turning point. This argument also explains why the small terms only become important in the region of S_c as it is here where $\frac{\partial f}{\partial x}|_{x_u}$ approaches zero (cf. (2.8)). Furthermore, it has been shown [5] that if the size of the small terms is $O(\epsilon)$ say, then the error in S_c is $O(\epsilon^{1/2})$, i.e. the difference in the predictions of S_c is always larger than the terms neglected in the LOM.

It was found that as $\zeta \to 1$ the range of S for which stable solutions exist increases dramatically and for certain values of S there are multiple stable solutions. As $\zeta \to 0$ the returning film thins and the comparison of these results with previous theoretical and experimental investigations for a SFF bead is of interest. These two limits are explored in detail below.

https://doi.org/10.1017/S0956792501004387 Published online by Cambridge University Press

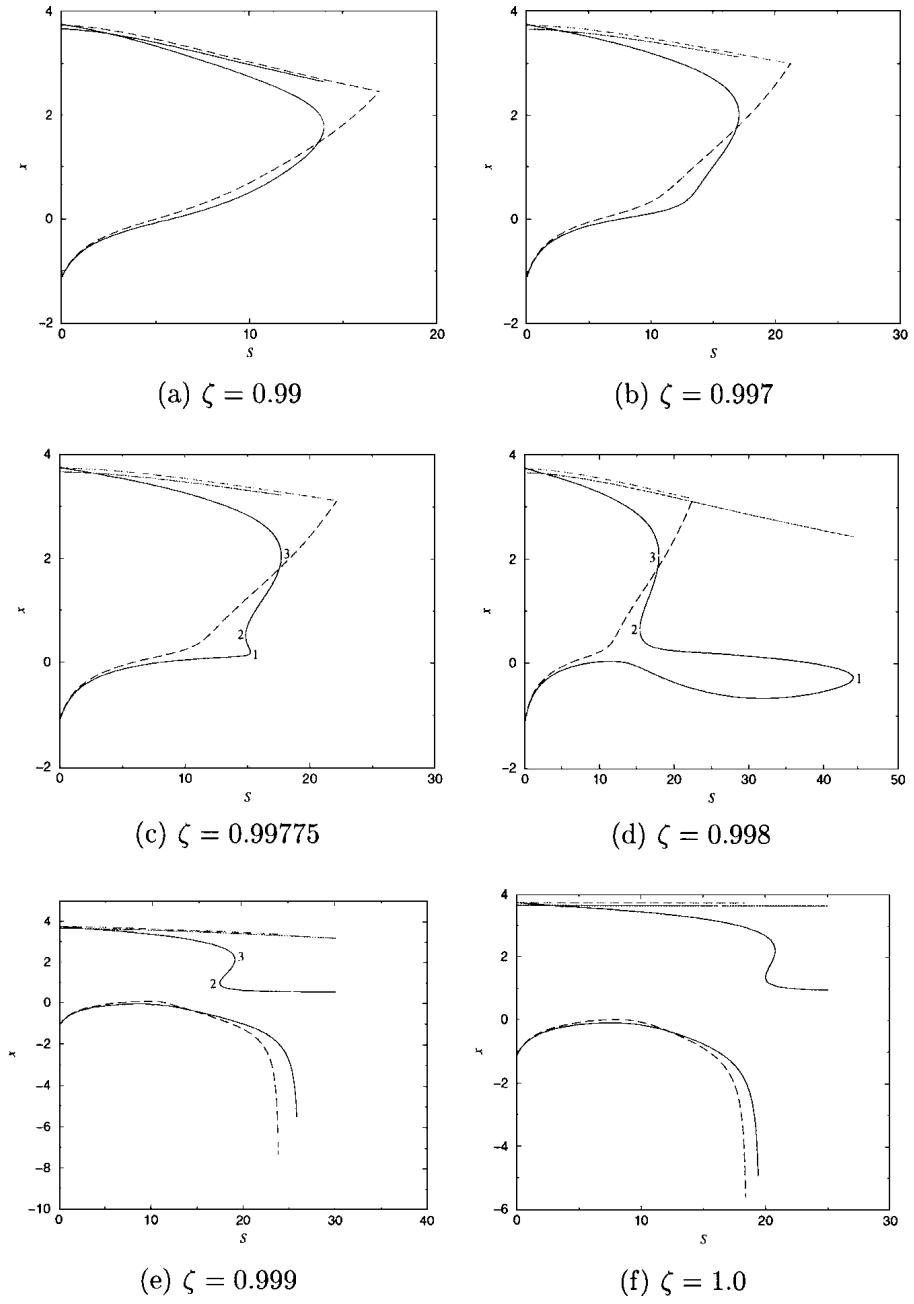

FIGURE 5. Menisci positions against S for different values of ζ. $Ca = 10^{-3}$, $\delta = 5 \times 10^{-3}$, $\lambda = 0.1$.

3.2 The limit $\zeta \to 1$

Figures 5(a) to (f) show menisci position plots for values of ζ ranging from 0.99 to 1.0. Figures 5(a) and (b), where $\zeta = 0.99$ and 0.997 respectively, are similar to Figure 4, and the turning point of the x_u solution curve is identified with the onset of bead break. The

https://doi.org/10.1017/S0956792501004387 Published online by Cambridge University Press

Table 1. *Values of* $\frac{q}{(1+S)}$. $Ca = 10^{-3}$, $\delta = 5 \times 10^{-3}$

λ	ζ	$\frac{q}{1+S}\|_{S_f}$
0.1	1.0	0.695
0.09	1.0	0.693
0.08	1.0	0.691
0.1	0.999	0.691

dashed curves again represent the LOM and here the difference in predictions of S_c is in the region of 25%. In Figure 5(c) the HOM predicts the x_u curve to have three, rather than one, turning points. According to (2.8), the sections of the curve below point 1 and between points 2 and 3 will be two-dimensionally stable, and thus for a small range of S there is no longer a unique two-dimensionally stable steady state. In addition, at point 1 the bead is neutrally stable, and if S is increased further then the bead could either collapse or jump to the section of the solution curve between points 2 and 3. Increasing ζ further leads to a dramatic increase in the 'lobe' between points 1 and 2, as Figure 5(d) shows, and then incrementing ζ still further gives rise to a change in the form of the x_u solution curve, i.e. it is no longer continuous – see Figure 5(e). It appears that there is a value of ζ at which the lobe 'snaps', and in Figure 5(e) the turning points analogous to those in Figure 5(c) have been labelled. Tracing the x_u solution curve from $S = 0$ in Figures 5(e) and (f) only temporarily results in bead contraction before it begins to expand again, and then at some value of S, S_f say, the upstream meniscus moves rapidly outwards – a feature which is identified as 'upstream flooding'. Despite the fact that three-dimensional instabilities cannot be ruled out in Figures 5(e) and (f) the plots do mimic the experimental results of Benkreira [2] and Benjamin [1], who investigated the flux through a DFF bead. Benjamin reported that for a DFF bead with $Ca = 0.83$ and $S = 1$, when the flux q equalled 1.315 the upstream interface flooded and the flow became three-dimensional. Benkreira measured the flux through a moderately starved DFF bead (steady and 2D) over a wide range of capillary numbers (10^{-2} – 10), and found it to be constant and equal to $0.651(1+S)$. These experimental results are similar to the theoretical value of $\frac{2}{3}(1+S)$ for the flux through a fully flooded pair of rolls, and suggest that when the flux through a DFF bead approaches this value then the inlet floods. Table 1 shows, for various values of λ and ζ, the value of $q/(1+S)$ for $S = S_f(\lambda, \zeta)$. The values are similar to those obtained experimentally, and provide the rationale for associating S_f, where the steady state solutions predict the upstream interface to move rapidly outwards, with the point of transition from a starved to moderately starved inlet. In each of Figures 5(e) and (f) there is a second branch of x_u solutions and in both cases this branch contains a section of two-dimensionally stable states, though it is only in the former that the two-dimensionally stable sections of each branch coexist over a range of S.

The two distinct phenomenon of bead break (figure 5(a)) and flooding (Figure 5(f)) are predicted by both the LOM and HOM and are supported by experiment. However, the states represented by Figures 5(b)–(e) differ so little in their values of ζ it is doubtful whether this intermediate behaviour could be demonstrated by experiment. In addition,

https://doi.org/10.1017/S0956792501004387 Published online by Cambridge University Press

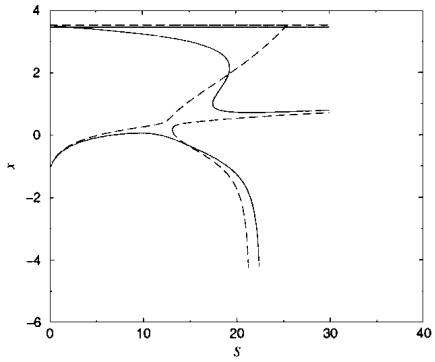

(a) $\lambda = 0.09$

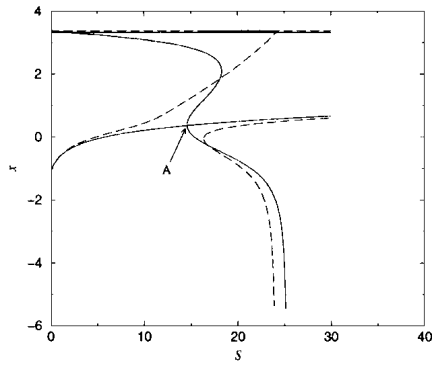

(b) $\lambda = 0.08323$

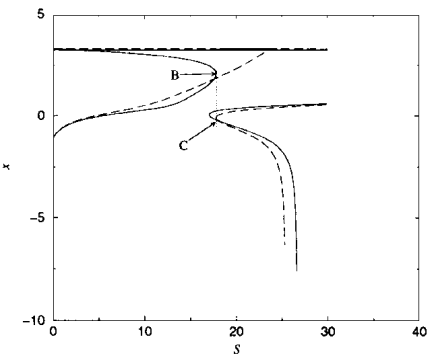

(c) $\lambda = 0.08$

FIGURE 6. Menisci locations against S for different values of λ. $Ca = 10^{-3}$, $\delta = 5 \times 10^{-3}$, $\zeta = 1.0$.

the route taken between bead break and flooding differs qualitatively between the models and it is unclear whether the effect of further terms would overide the significant changes shown here in the HOM predictions due to slight changes in ζ. Despite this, Figures 5(b)–(e) do serve to illustrate how the physical transition from bead break to flooding is predicted according to the LOM and HOM, which represent successive refinements to an asymptotic theory, and highlight the possibility of multiple stable states during this

https://doi.org/10.1017/S0956792501004387 Published online by Cambridge University Press

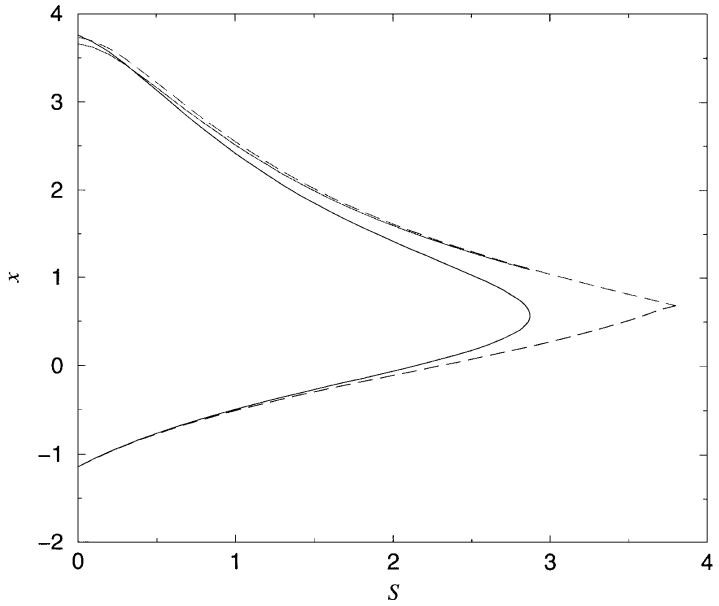

FIGURE 7. Menisci locations against S. $Ca = 10^{-3}$, $\delta = 5 \times 10^{-3}$, $\lambda = 0.1$, $\zeta = 0.01$.

transition. It should be noted that the next refinement to the model (i.e. the $O(Ca)$ correction to the boundary conditions) would require a numerical solution to the flow field and is beyond the scope of this paper.

Figures 6(a)–(c) are meniscus location plots for $\zeta = 1$, each at a different values of λ. Figure 6(a) is similar to Figures 5(e) and (f), there are two branches for x_u, with the lower one exhibiting upstream flooding behaviour. When λ is decreased to the critical value of 0.8323 the two branches join as in Figure 6(b). Here, as S is increased from zero, the bead gradually contracts until point A is reached, beyond which there are three local choices for x_u, the upper and lower choices initially being two-dimensionally stable and eventually leading to bead break and flooding, respectively. Clearly, a three-dimensional stability analysis is needed to determine which path is taken as S is increased beyond point A. As λ is decreased further there are again two branches, see Figure 6(c). In this case, increasing S from zero leads to the upstream interface moving downstream, passing through the nip and reaching the critical point B where the bead becomes two-dimensionally neutrally stable and could either collapse or jump to the point C, whereby further increases in S would lead to flooding.

3.3 The limit $\zeta \to 0$

Figure 7 shows a typical plot for a small value of ζ. All the menisci location plots generated at low values of ζ have this form and the differences in the predicted value of S_c between the HOM and the LOM was in the region of 35%. The interest here lies in the comparisons with both the modelling and experiments for the SFF system.

The downstream meniscus location, x_d, is determined by balancing incoming and outgoing fluxes so that when $\zeta \ll 1$ the returning film plays a negligible role and the

https://doi.org/10.1017/S0956792501004387 Published online by Cambridge University Press

Table 2. *Comparison with contact angle results*

ζ	Effective contact angle
0.025	2.98^o
0.01	12.22^o
0.001	30.57^o
0.0001	57.37^o

result would be very close to that of the SFF model. The upstream location, x_u, is determined by balancing capillary and hydrodynamic pressures and in the SFF model the capillary pressure is a function of the imposed contact angle, so it is therefore possible to vary this contact angle until the HOM and the SFF model give the same pressure drop across the upstream interface and hence the same value of x_u. Table 2 shows this 'effective contact angle' for various small values of ζ.

When $\zeta = 0.025$ the effective contact angle is small, as would be expected with the presence of a returning film. However, as ζ is decreased the effective contact angle grows significantly and when $\zeta = 10^{-4}$ it is 57.37^o. During the experiments of Kapur [6], the upper roll was scraped in an attempt to replicate a dry incoming surface, however the scraping leaves behind a thin residual film whose thickness is less than 1% of the outgoing film. In these experiments 'apparent contact angles' in the region of 50^o were found, in agreement with the effective contact angles described above. Thus, the HOM, with small ζ, produces results in accord with the SFF model with realistic imposed contact angles, and could therefore form the basis of a precursor film model for such systems, removing the inherent difficulties associated with modelling the contact line.

The reason why the HOM, a model for the DFF bead, is capable of producing pressure drops at the upstream meniscus similar to the SFF model is due to the form of the constant $\mathscr{A}_2$ in (2.7). $\mathscr{A}_2$ becomes large and negative as $\zeta \to 0$ so the 'small' corrections to ΔP_u become more significant in this limit and eventually the ordering of the series breaks down and results are no longer obtainable.

4 Conclusions

It is clear that the correction terms, derived in Appendix A, are vital in accurately predicting the critical operating conditions of a multi-roll coater, and in particular the event of bead break. The inclusion of the small terms can lead to a difference of up to 35% in the prediction of S_c.

As $\zeta \to 1$ it is possible for the upstream interface position to move rapidly outwards as S is increased, and this is associated with flooding. The precise values of ζ and λ dictate whether the bead will collapse or flood as S is increased, and under certain conditions a pair of solution branches exist, one exhibiting bead break behaviour and the other flooding behaviour. Three-dimensional instabilities cannot be ruled out in this region of parameter space, however the predictions of flooding agree qualitatively with experimental results.

In the limit $\zeta \to 0$, the small terms play an important role in modelling the pressure

https://doi.org/10.1017/S0956792501004387 Published online by Cambridge University Press

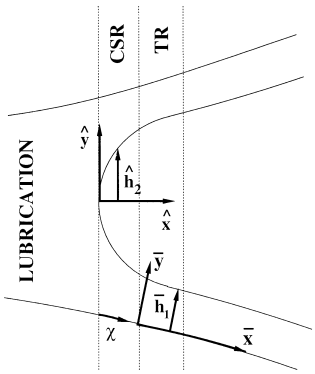

FIGURE A 1. Regions and axes at downstream meniscus.

jump at the upstream interface. The calculated effective contact angles are in agreement with observed apparent contact angles.

Appendix A

To find the pressure drops across the interfaces and the outgoing film thicknesses, the flow in the vicinity of the menisci needs to be considered. This is achieved at each interface in turn by analysing a Capillary Statics Region (CSR), where capillary forces are dominant, and a Transition Region (TR), where capillary forces balance the viscous forces which dominate in the thin films far from the bead, and then matching the solutions of the two regions. These regions at the downstream meniscus are illustrated in Figure A 1.

Suitable scalings in the region of the downstream meniscus are:

$$X \sim B_D, \quad Y \sim B_D, \quad \mathbf{u} \sim U_2, \quad B(X) \sim B_D, \quad P \sim \sigma/B_D,$$

where $\mathbf{u}$ is the velocity field and $B_D = B(X_D) = R + B_0 - \sqrt{R^2 - X_D^2}$, and hence the solution in this region is dependent upon X_D.

After shifting the origin to the tip of the downstream meniscus and rescaling the variables the continuity equation and equation of motion in the vicinity of this interface are

$$\hat{\nabla}.\hat{\mathbf{u}} = 0, \qquad \hat{\nabla}\hat{p} = Ca\hat{\nabla}^2\hat{\mathbf{u}}, \tag{A 1}$$

and the normal stress balance is

$$\hat{p}_a - \hat{p} = \Delta\hat{P} = \frac{-\hat{h}_{\hat{x}\hat{x}}}{(1+\hat{h}_{\hat{x}}^2)^{\frac{3}{2}}} + O(Ca) \quad \text{on} \quad \hat{y} = \hat{h}. \tag{A 2}$$

$\hat{p}_a$ is the atmospheric pressure and $\hat{h}(\hat{x})$ represents the free surface profile. Variables in this region, that have been non-dimensionalised as above, will be denoted by a 'hat'. (A 1) states that viscous forces are negligible in this region and thus only the pressure and free surface profile are solved for, leaving the flow field unknown. Equation (A 2) is a differential equation for $\hat{h}$ containing an unknown constant, $\Delta\hat{P}$. As $\hat{h}(\hat{x})$ is double valued we will split it into 'lower' and 'upper' branches, $\hat{h}_1(\hat{x})$ and $\hat{h}_2(\hat{x})$ associated with the lower and upper rolls, respectively. The formulation of the problem in this region is completed

https://doi.org/10.1017/S0956792501004387 Published online by Cambridge University Press

by imposing the following boundary conditions:

$$\hat{h}_1(\hat{x}=0) = \hat{h}_2(\hat{x}=0) = \hat{r}, \tag{A 3}$$

$$\hat{h}_{1_{\hat{x}}}(\hat{x}=0) = -\hat{h}_{2_{\hat{x}}}(\hat{x}=0) = -\infty, \tag{A 4}$$

where (A 3) allows the solution to be asymmetric via the unknown constant $\hat{r}$ and (A 4) implicitly defines the origin of the CSR as the 'turing point' of the meniscus.

In the TR the fluid is drawn from the meniscus into thin films on each roll surface, and thus here it is natural to adopt a curvilinear coordinate system $(\overline{x}, \overline{y})$ as shown in Figure A 1 for the lower roll. A similar coordinate system associated with the upper roll exists, the analysis below holds for both rolls. Following previous workers the scales in this region, derived by balancing capillary and viscous stresses, are

$$P \sim \sigma/B_D, \quad U \sim U_2, \quad V \sim Ca^{1/3}U_1, \quad Y, H \sim Ca^{2/3}B_D, \quad X \sim Ca^{1/3}B_D,$$

and variables that have been non-dimensionalised with these scales are denoted by a 'bar'. In the following, $(\overline{x}, \overline{y})$ refer to the TR coordinates on either roll. Neglecting terms of $O(Ca^{2/3})$ the governing equations and boundary conditions become

$$\frac{\partial \overline{p}}{\partial \overline{x}} = \frac{\partial^2 \overline{u}}{\partial \overline{y}^2}, \qquad \frac{\partial \overline{p}}{\partial \overline{y}} = 0, \tag{A 5}$$

$$\frac{\partial \overline{u}}{\partial \overline{y}}\Big|_{\overline{y}=\overline{h}_i} = 0, \qquad \overline{u}|_{\overline{y}=0} = \kappa_i, \tag{A 6}$$

where $i = 1$ and $i = 2$ differentiate between the analysis of the lower and upper rolls, respectively, therefore $\kappa_1 = 1$ and $\kappa_2 = S$.

The two regions are linked by matching the perpendicular distance between the roll surface and the interface. In the TR this quantity is simply given by $\overline{h}_i$ whereas in the CSR, where it is denoted by $\hat{h}_{\perp_i}$, it is given by

$$\hat{h}_{\perp_i}(\hat{x}) = (\hat{b}(\hat{x}) - (-1)^i \hat{h}_i(\hat{x}))(1 + \hat{x}_d^2\delta^2(\tfrac{1}{2} - 2\hat{x})) + O(\delta^3). \tag{A 7}$$

The semi-gap width relative to the CSR coordinates is $\hat{b}(\hat{x}) = 1 + 2\hat{x}x_d\delta + x^2 b_d^2\delta^2$. To facilitate the matching process it is useful to write $\hat{h}_{\perp_i}$ in terms of an arclength coordinate χ, shown in Figure A 1, and given by

$$\chi = \hat{x}(1 - 2\hat{x}_d^2\delta^2\hat{x}) + O(\delta^3). \tag{A 8}$$

This allows Van Dyke's matching rule to be used, resulting in

$$\lim_{\chi \to \hat{l}_i} \hat{h}_{\perp_i} = \lim_{\overline{x} \to -\infty} Ca^{2/3}\overline{h}_i, \tag{A 9}$$

where $\hat{x} = \hat{l}_i$ is the origin of the TR. This matching condition is utilised by first expanding $\hat{h}_i$ about $\chi = \hat{l}_i$, secondly rewriting the expansion in terms of $\overline{x}$, and finally, by expanding the resultant expression about $\hat{l}_i^{00}$.

A solution in the form of a double expansion in the small parameters $Ca^{1/3}$ and δ is now sought:

$$p = p^{00} + Ca^{1/3}p^{10} + \delta p^{01} + Ca^{1/3}\delta p^{11} + Ca^{2/3}p^{20} + \ldots, \tag{A 10}$$

$$h = h^{00} + Ca^{1/3}h^{10} + \delta h^{01} + Ca^{1/3}\delta h^{11} + Ca^{2/3}h^{20} + \ldots. \tag{A 11}$$

https://doi.org/10.1017/S0956792501004387 Published online by Cambridge University Press

In the capillary statics region the flow field is not solved for, therefore asymmetries due to $S \neq 1$ only enter the problem via the transition region. However, the transition region enters the matching process at $O(Ca^{2/3})$ so until then the capillary statics solution must be symmetric and in particular $\hat{r}^{00} = 0$. Furthermore, the effect of the non-constant gap width enters at $O(\delta)$ so at $O(1)$ and $O(Ca^{1/3})$ the capillary statics region problem is exactly analogous to the Hele–Shaw cell problem discussed by Park & Homsy [12], who found that $\Delta\hat{P}^{00} = 1$, $\hat{l}_i^{00} = 1$ and the surface profile at leading order to be

$$\hat{h}_i^{00} = (-1)^i(1 - (1 - \hat{x})^2)^{\frac{1}{2}}. \tag{A 12}$$

They also found that $\Delta\hat{P}^{10} = 0$, implying that $\hat{h}_i^{10} \equiv 0$. The normal stress balance at $O(Ca^{2/3})$ is

$$\Delta\hat{P}^{20} = (-1)^{i+1}\left[\frac{\hat{h}_{i_{\hat{x}}}^{20}}{(1 + \hat{h}_{i_{\hat{x}}}^{00^2})^{3/2}}\right]_{\hat{x}}, \tag{A 13}$$

with solution

$$\hat{h}_i^{20} = (-1)^{i+1}\frac{\hat{x}\Delta\hat{P}^{20}}{(1 - (1 - \hat{x})^2)^{\frac{1}{2}}} + \hat{r}^{20}, \tag{A 14}$$

and $\Delta\hat{P}^{20}$ and $\hat{r}^{20}$ are found from matching with the leading order solution from the TR derived below.

Equation (A 5) can be solved, subject to (A 6), to produce the familiar Landau Levich equation

$$\overline{h}_{i_{\overline{x}\overline{x}\overline{x}}}^{00} = 3\kappa_i\frac{\overline{t}_i^{00} - \overline{h}_i^{00}}{\overline{h}_i^{00^3}}, \tag{A 15}$$

where $\overline{t}_i$ is the final film thickness. Making the transformation

$$\overline{X} = -(3\kappa_i)^{1/3}\frac{\overline{x} + \overline{s}_i}{\overline{t}_i^{00}}, \qquad \overline{H}_i = \frac{\overline{h}_i^{00}}{\overline{t}_i^{00}}, \tag{A 16}$$

leads to

$$\overline{H}_{i_{\overline{X}\overline{X}\overline{X}}}^{00} = \frac{\overline{H}_i^{00} - 1}{\overline{H}_i^{00^3}}, \tag{A 17}$$

which has no dependency on S, thus $\overline{H}_1 \equiv \overline{H}_2$ and the subscripts are dropped hereafter. Imposing $\overline{H}^{00} \to \infty$ as $\overline{X} \to \infty$ and $\overline{H}^{00} \to 1$ as $\overline{X} \to -\infty$, leads to

$$\begin{array}{lll} \overline{H}^{00} & \sim & \frac{1}{2}C_0\overline{X}^2 + C_1\overline{X} + C_2 \qquad \text{as } \overline{X} \to \infty, \\ \overline{H}^{00} & \sim & 1 + Ae^{\overline{X}} \qquad\qquad\qquad\quad \text{as } \overline{X} \to -\infty. \end{array} \tag{A 18}$$

$\overline{s}_i$ is chosen such that C_1 is zero whilst A, C_0 and C_2 are determined by numerical integration of (A 17), and their values are 0.862, 0.643 and 2.895, respectively.

https://doi.org/10.1017/S0956792501004387 Published online by Cambridge University Press

The CSR solution first enters the matching process at $O(Ca^{2/3})$:

$$(-1)^i\left(\frac{\overline{x}^2}{2}\hat{h}^{00}_{i_{\hat{x}\hat{x}}}(\hat{l}^{00}_i)+\overline{x}\hat{l}^{10}_i\hat{h}^{00}_{i_{\hat{x}\hat{x}}}+\frac{1}{2}\hat{l}^{10^2}_i\hat{h}^{00}_{i_{\hat{x}\hat{x}}}(\hat{l}^{00}_i)+\hat{h}^{20}_i(\hat{l}^{00}_i)\right)$$
$$=(3\kappa_i)^{2/3}\frac{C_0}{2\bar{t}^{00}_i}\overline{x}^2+(3\kappa_i)^{2/3}\frac{C_0}{\bar{t}^{00}_i}\overline{x}\overline{s}_i+C_2\bar{t}^{00}_i+(3\kappa_i)^{2/3}\frac{C_0}{2\bar{t}^{00}_i}\overline{s}_i^2. \tag{A 19}$$

Note the fact that $\hat{h}_{i_{\hat{x}}}(\hat{l}^{00}_i)=0$ has been used. The $\overline{x}^2$ terms give $\bar{t}^{00}_i=(3\kappa_i)^{2/3}C_0$ and the $\overline{x}$ terms lead to $\hat{l}^{10}_i=\overline{s}_i$. Since $\hat{l}^{10}$ represents a correction to the origin of the TR, this implies that the solution is independent of $\overline{s}_i$. The results of the remaining constant terms are

$$\Delta\hat{P}^{20}=C_0C_2\frac{3^{2/3}}{2}(1+S^{2/3}), \tag{A 20}$$

$$\hat{r}^{20}=C_0C_2\frac{3^{2/3}}{2}(1-S^{2/3}). \tag{A 21}$$

Substituting (A 20) and (A 21) into (A 14) gives the leading order asymmetrical contribution to the CSR free surface profile.

The non-constant gap width corrections which enter the problem at $O(\delta)$ are now calculated. The $O(\delta)$ solution is similar in form to (A 14), the $O(Ca^{2/3})$ solution. Now the $O(\delta)$ matching condition is

$$2x_d-(-1)^i\hat{h}^{01}_i(\hat{l}^{00}_i)-(-1)^i\hat{l}^{01}\hat{h}^{00}_{i_{\hat{x}}}(\hat{l}^{00})=0, \tag{A 22}$$

the first term coming from the $\hat{b}$ contribution to $\hat{h}_{\perp_i}$. This condition gives us $\Delta\hat{P}^{01}=-2x_d$ and $\hat{r}^{01}=0$. Thus, the correction due to the non-constant gap is simply proportional to the gradient of the gap where the meniscus forms and the solution is symmetric at this order.

As for the TR, the order δ problem, after a transformation similar to (A 16), is

$$\overline{H}^{01}_{\overline{X}\overline{X}\overline{X}}=\frac{3\overline{H}^{01}-2\overline{H}^{00}\overline{H}^{01}-\overline{H}^{00}R}{\overline{H}^{00^4}} \tag{A 23}$$

where $R=\bar{t}^{01}_i/\bar{t}^{00}_i$. The asymptotic behaviour of $\overline{H}^{01}$ is

$$\begin{aligned}\overline{H}^{01}_i &\sim \tfrac{1}{2}D_0\overline{X}^2+D_1\overline{X}+D_2 \qquad \text{as } \overline{X}\to\infty,\\ \overline{H}^{01}_i &\sim R+(B-RA\overline{X})e^{\overline{X}} \qquad \text{as } \overline{X}\to-\infty.\end{aligned}$$

As the $O(1)$ solution is independent of $\overline{s}_i$, it can be chosen so that $D_1=0$. Thus there are four unknown constants D_0, D_2, B and R and numerical integation of the third order equation (A 23) gives

$$R=-1.556D_0,\quad B=-0.853D_0,\quad D_2=-2.04D_0. \tag{A 24}$$

Note that the behaviour for large negative $\overline{X}$ differs from that stated by Park & Homsy [12] as they omitted the final term on the right-hand-side. The $O(Ca^{1/3}\delta)$ matching condition is

$$-(-1)^i(\hat{h}^{11}_i(\hat{l}^{00}_i)+\hat{l}^{10}_i\hat{h}^{01}_{i_{\hat{x}}}(\hat{l}^{00}_i)+\hat{l}^{10}_i\hat{l}^{01}_i\hat{h}^{00}_{i_{\hat{x}\hat{x}}}(\hat{l}^{00}_i)+\overline{x}\hat{h}^{01}_{i_{\hat{x}}}(\hat{l}^{00}_i)+\overline{x}\hat{l}^{01}\hat{h}^{00}_{i_{\hat{x}\hat{x}}}(\hat{l}^{00}_i))=0, \tag{A 25}$$

giving $\hat{l}^{01}_i=2x_d$, $\Delta\hat{P}^{11}=0$, $\hat{r}^{11}_i=0$, and therefore $\hat{h}^{11}_i\equiv 0$. Thus, there is no correction

https://doi.org/10.1017/S0956792501004387 Published online by Cambridge University Press

to the pressure jump at this order, but there is a correction to the location of the origin of the TR due to the slope of the rollers. The $\bar{x}^2$ terms from the $O(Ca^{2/3}\delta)$ matching condition give

$$D_0 = -2x_d\bar{t}_i^{00}/(3\kappa_i)^{2/3} \tag{A 26}$$

which in turn gives $\bar{t}_i^{01} = 2x_dC_0(3\kappa_i)^{2/3}$. Park & Homsy [12] showed that $\bar{t}_i^{10} = 0$.

Thus the downstream pressure jump and outgoing film thicknesses are of the following form:

$$\Delta\hat{P}_d = 1 - 2x_d\delta + 1.94(1 + S^{2/3})Ca^{2/3} + O(Ca, \delta^2, Ca^{2/3}\delta), \tag{A 27}$$

$$\bar{t}_i = 1.337\kappa_i^{2/3}(1 + 2x_d\delta) + O(Ca^{2/3}, \delta^2, Ca^{1/3}\delta). \tag{A 28}$$

The analysis for the upstream menisci is largely similar to that of the upstream. The first difference is that x_d needs to be replaced by $-x_u$ as this is the distance from the nip to the upstream interface. The second difference enters via the no slip boundary conditions on the roll surfaces used in the TR analysis, since at the downstream interface the thin films are being pulled from the bead whereas at the upstream interface they are being pushed into the bead. At leading order the equivalent equation to (A 15) is:

$$\bar{h}^{00}_{i_{\bar{x}\bar{x}\bar{x}}} = -3\kappa_i\frac{\bar{t}_i^{00} - \bar{h}_i^{00}}{\bar{h}_i^{00^3}}. \tag{A 29}$$

Making the transformation

$$\overline{X} = (3\kappa_i)^{1/3}\frac{\bar{x} + \bar{s}_i}{\bar{t}_i}, \qquad \overline{H}_i = \frac{\bar{h}_i}{\bar{t}_i}, \tag{A 30}$$

where $\bar{t}_i$ now represents the thickness of the incoming films, results in (A 17). However, this time we require the solution to decay as $X \to \infty$ rather than as $X \to -\infty$, as was the case at the downstream meniscus. This means that the asymptotic behaviour of $\overline{H}_i^{00}$ is

$$\begin{aligned} \overline{H}_i^{00} &\sim \tfrac{1}{2}E_{0_i}\overline{X}^2 + E_{2_i} && \text{as } X \to -\infty, \\ \overline{H}_i^{00} &\sim 1 + e^{-\overline{X}/2}(I_i\cos\tfrac{\sqrt{3}}{2}\overline{X} + J_i\sin\tfrac{\sqrt{3}}{2}\overline{X}) && \text{as } X \to \infty. \end{aligned}$$

Note that this is a third order equation with boundary conditions containing four unknowns, thus three of the unknowns can be found as functions of the fourth via numerical integration of (A 17). Figure A 2 shows E_2 as a function of E_0.

The matching condition at $O(Ca^{2/3})$, at the upstream interface, is similar to (A 19) with the $\bar{x}^2$ terms producing:

$$E_{0_1} = \frac{2\lambda}{(3Ca)^{2/3}b_u}, \qquad E_{0_2} = \frac{b_d}{b_u}\zeta C_0. \tag{A 31}$$

The constant terms give:

$$\Delta\hat{P}_u^{02} = \frac{\lambda}{Ca^{2/3}b_u}E_{2_1} + \frac{b_d\zeta(3S)^{2/3}C_0}{2b_u}E_{2_2}, \tag{A 32}$$

$$\hat{r}^{20} = \frac{\lambda}{Ca^{2/3}b_u}E_{2_1} - \frac{b_d\zeta(3S)^{2/3}C_0}{2b_u}E_{2_2}. \tag{A 33}$$

https://doi.org/10.1017/S0956792501004387 Published online by Cambridge University Press

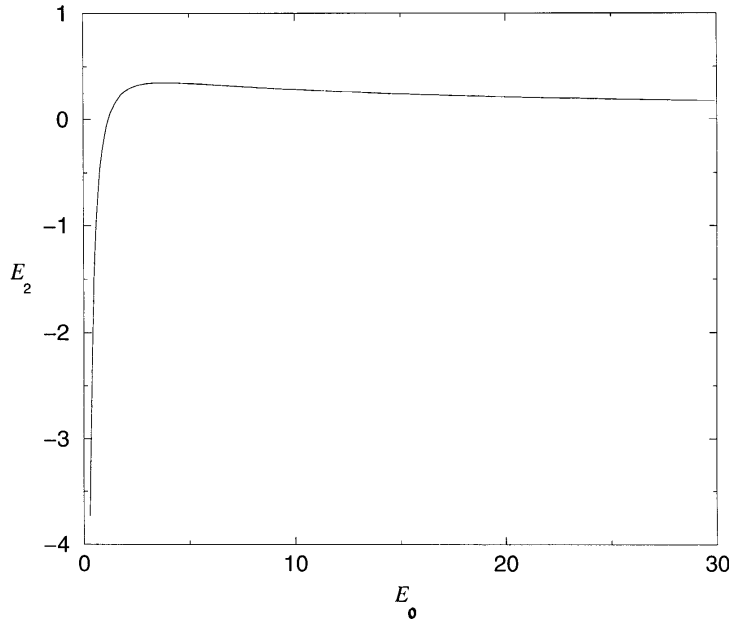

FIGURE A 2. E_2 against E_1.

Therefore, the pressure jump at the upstream interface is

$$\Delta\hat{P}_u = 1 + 2x_u\delta + \frac{\lambda}{b_u}E_{2_1} + \frac{b_a\zeta(3S)^{2/3}C_0}{2b_u}E_{2_2}Ca^{2/3}. \tag{A 34}$$

References

[1] BENJAMIN, D. F. (1994) Roll coating flows and multiple roll systems. *PhD thesis*. University of Minnesota.

[2] BENKREIRA, M. F., EDWARDS, M. F. & WILKINSON W. L. (1981) Roll coating of purely viscous liquids. *Chem. Eng. Sci.* **36**, 429–34.

[3] BRETHERTON, F. P. (1961) The motion of long bubbles in tubes. *J. Fluid Mech.* **10**, 166–188.

[4] DANIELS, N. (1998) Instabilities in roll and slot coating flows. *PhD thesis*, University of Leeds.

[5] GOSTLING, M. J. (2000) Instabilities in rigid and deformable roll coating. *PhD thesis* (in preperation), University of Leeds.

[6] KAPUR, N. (1999) Flow phenomena in fixed-gap and gravure roll coating systems. *PhD thesis*, University of Leeds.

[7] KAPUR, N., GASKELL, P. H. & SAVAGE, M. D. (2000) Bead break instability. *Phys. Fluids* (accepted).

[8] LANDAU, L. & LEVICH, B. (1942) Dragging of a liquid by a moving plate. *Acta Physicochimica U.R.S.S.* **XVII**(1–2), 42–54.

[9] MALONE, B. (1992) An experimental investigation of roll coating phenomena. *PhD thesis*, University of Leeds.

[10] MICHALLAND S. (1992) Etude des differents regimes dynamiques de l'instabilite de l'impremeur. *Thesis L'Ecole Normale Superieure*, Paris.

[11] MICHALLAND S., RABAUD, M. & COUDER, Y. (1996) Instabilities of the upstream interface in directional viscous fingering. *J. Fluid Mech.* **312**, 125–148.

[12] PARK, C. W. & HOMSY, P. H. (1984) Two-phase displacement in Hele Shaw cells: theory. *J. Fluid Mech.* **139**, 291–308.

[13] Rabaud, M., Michalland S. & Couder, Y. (1990) Dynamical regimes of directional viscous fingering – spatiotemporal chaos and wave propagation. *Phys. Rev. Lett*. **64**, 184–87.
[14] Reinelt, D. A. (1995) The primary and inverse instabilities of directional viscous fingering. *J. Fluid Mech*. **285**, 303–327.

https://doi.org/10.1017/S0956792501004387 Published online by Cambridge University Press